ASME Journal of Electrochemical Energy Conversion and Storage
Online journal at:
https://asmedigitalcollection.asme.org/electrochemical

Enhancing the Thermal Dissipation in Batteries via Inclusion of Central Heat Sink

Asghar Aryanfar[1]
Department of Mechanical Engineering,
Bogazici University,
Bebek, Istanbul 34342, Turkey
e-mail: aryanfar@caltech.edu

Fadi Elias
Department of Mechanical Engineering,
American University of Beirut,
Riad El-Solh, Beirut 1107 2020, Lebanon
e-mail: fse09@mail.aub.edu

William A. Goddard III
Department of Applied Physics,
California Institute of Technology,
1200 East, California Boulevard,
Pasadena, CA 91125
e-mail: wag@caltech.edu

The generation of heat within the rechargeable batteries during the charge–discharge cycles is inevitable, making heat dissipation a very critical part of their design and operation procedure, as a safety and sustainability measure. In particular, when the heat gets the least possibility to escape from the electrode surface, the boundary of the packaging material remains the sole heat dissipator. In this regard, the heat gets accumulated in the central zone, making it the most critical, since it has the least possibility to escape to the surroundings. Anticipating such a heat trap, a central heat sink component is devised, where the role of its conductivity and the relative scale is analyzed based on the formation of transient and steady-state temperature profiles. Additionally, an analytical solution is attained for the location of the maximum temperature, where its value and correlation with the electrolyte conductivity, heat generation rate, and scale of the cell have been quantified. Due to the existence of the curved boundaries, it is shown that the time versus space resolution for capturing the transient evolution of the temperature is more strict than the flat surface and analytically acquired as ≈33% smaller value. Such enhanced design and subsequent analysis are critical for planning sustainable and cost-effective packaging to avoid the ignition and failure of the respective electrolyte. [DOI: 10.1115/1.4062712]

Keywords: heat dissipation, design and analysis, batteries, thermal management, analytical solution, numerial simulation

1 Introduction

Everyday technology is tending to moderate itself at exponential rates [1]. While energy-sourcing from traditional fossil fuels has proven not to be environmentally friendly, the new electric-powered age has been initiated in recent decades. Furthermore, with the increasing involvement of silicon-based portables in daily life, the demand for electric power has become very critical. In order to meet this call, it is imperative to equip the electric power sources with the greatest amount of energy density, which could get utilized over an extensive period [2,3]. The rechargeable lithium-based battery is a clean and dense source of electric energy in this regard, which operates fundamentally via chemical reactions to generate electric current and can get scaled up to acceptable sizes and designs for optimal comfort in electronics and transportation [4,5].

However, the chemical reaction is exothermic, meaning that energy is released in the process, which heats the battery, and if not dissipated systematically, it leads to a thermal runaway in the electrolyte, causing safety hazards [6].

The techniques for the thermal management of rechargeable batteries have explored packaging [7], calorimetry [8,9], external heating [10], local heating [11], heat flux measurement [12], over-reaction [13], respective irregularities [14], capacity decay [15], development of a machine learning method to estimate the state of health [16], discharge methodology [17], overcharge-analysis [18], and designing temperature resilient electrolytes [19].

Previous research works have analyzed thermal management in packing [20], design and adoption of heat-dissipating mini-channels [21], heat dissipation design [22], real-time temperature monitoring [23], and heat treatment for the purpose of recycling [24].

Several works have investigated the variable heat dissipation rate due to unidirectional flow [25], non-invasive predicted the internal temperature from boundary conditions [26], and explored the radial variation in the thermal conductivity [27]. On a larger scale, heat pipes have been extensively utilized [28] and redesigned [29], where transient heat transfer has been predicted for high discharge rates [22]. Particularly, pulsating heat pipes (PHP), which possess high heat transfer efficiency, are utilized in electronics cooling and waste heat recovery [30]. Moreover, the liquid cooling channels have been micro-architected in the pouch cell configuration [31] and analyzed versus channel size, inlet temperature, and inlet flow velocity [32]. As well, the utilization of phase change materials (PCM) has been explored as an efficient temperature control tool for safe operation in low-temperature range and is optimized versus the fin number and shape of the module [33].

Thus, new methods of development of batteries have been adapted, in terms of cost-effective geometrical designs, mainly due to the cost-effectiveness of a one-time installment. This has already been adapted and is trending in the electronic world, specifically in the coin cell, which has the possibility of scalability, particularly for stationary applications. New designs are proposed to

[1]Corresponding author.

Manuscript received December 27, 2022; final manuscript received June 4, 2023; published online June 26, 2023. Assoc. Editor: Ankur Jain.

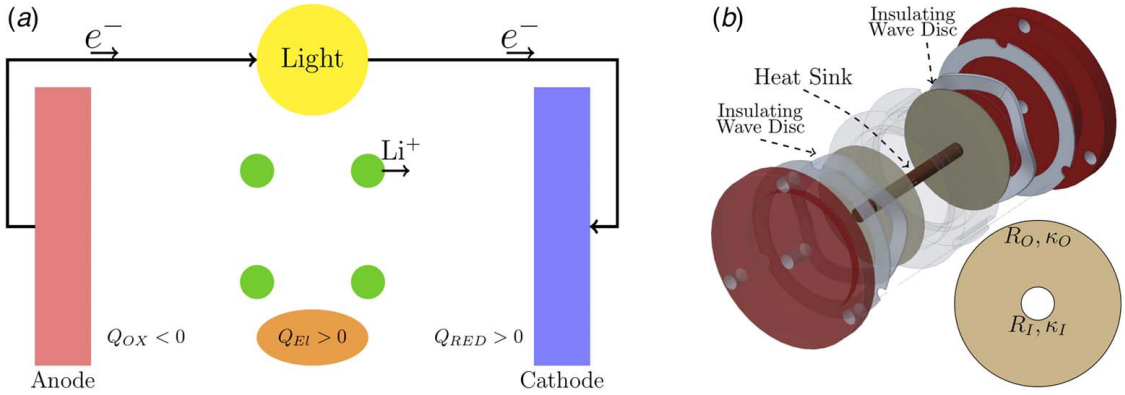

Fig. 1 Heat generation and respective design for the central dissipation

optimize multiple factors, including component compatibility [34], primarily by requiring a minimal amount of material, considering the operational limitations. Furthermore, they excel in their reproducibility on large scales, simple bulk production, described by minimal dimensional conditions, generating remarkable capability and simplicity in testing. However, the overheating and ignition at the vicinity of flash point temperature remains a vital problem to overcome and optimize.

This paper tackles the most critical heat zone of the electrode-sealed sandwich cell battery, which is located at the central zone and carries the least heat dissipation. Therefore, a highly heat-conducting rod is devised, which absorbs the accumulated thermal energy and forks it out from the perpendicular direction to the environment. Subsequently, the role of the material type and the relative scale of the heat sink is explored in the formation of the ultimate temperature profile, where the flash temperature of the electrolyte could be avoided. Moreover, attaining healthier heat management for the battery opens the possibility of the use of low heat-diffusivity sustainable packaging materials, which are typically more recyclable and economical [35,36].

2 Methodology

Figure 1(*a*) illustrates the ionic reaction and transport within the electrolyte. Although the oxidation and the reduction reactions are endothermic and exothermic with the same rate, neutralizing each other, the generated energy rate $\dot{q}_{GEN}$ (i.e., heating up) is caused by the transport of the ions within the electrolytic medium. For the circular electrode, $T(r,\ t)$ represents the temperature at the radial distance r and the time t; therefore, the temperature evolution is governed as [37]

$$\frac{\partial T}{\partial t} = \alpha\left(\frac{\partial^2 T}{\partial r^2} + \frac{1}{r}\frac{\partial T}{\partial r}\right) + \frac{\dot{q}_{GEN}}{\rho c} \tag{1}$$

where r is the radial distance, that is confined between the inner and outer radii ($R_I \le r \le R_O$), α, ρ, and c are the heat diffusivity, mass density, and the specific heat capacity of the electrolyte. The rate of heat generation per unit volume $\dot{q}_{gen}$ is in fact the work of the drag force $F_d = 6\pi\mu a v$ on the charge carriers with the radius a as [38]

$$\dot{q}_{GEN} = \frac{F_d l}{Alt} N = \frac{6N\pi\mu a}{Al} v^2 \tag{2}$$

where l, t, and v are the distance, the time, and the velocity of ionic transfer in the inter-electrode space, respectively, N is Avogadro's number, and μ is the viscosity of the electrolyte. Having the current relationship as $Q = iAt$, Eq. (2) is rewritten as

$$\dot{q}_{GEN} = 6\pi A\mu a N l\left(\frac{i}{Q}\right)^2 \tag{3}$$

where i is the current density, A is the electrode area, and Q is the amount of the transferred charge. The generated heat is typically transported to the boundaries and gets dissipated there. While such dissipation is more feasible for the boundary regions, mainly due to accessibility, it is the most difficult for the center to dissipate heat, and as a result, there is more heat accumulation in those regions. We could overcome the temperature accumulation in the center by anticipating a heat-dissipating element as illustrated in Fig. 1(*b*). Such an element could be a thin rod of certain conductivity, which is aligned in the perpendicular (in/out of plane) direction to the electrodes, providing the access to environment of the ambient temperature. Therefore, it could fork out the trapped heat locally from the central zone. While the respective thermal conductivity of the rod could vary, the metal choice would require insulation from the electrode and current collectors in their connections by means of plastic sleeves. As well, the scale of the rod element could in fact be very small, compared to the rest of the battery, since the central region has a relatively smaller area and generated heat. Assuming the radii of the central element and the domain are R_I and R_O, respectively, the boundary conditions will be the heat transfer rate in the inner and outer surfaces that correlates with the respective temperature gradients (i.e., $\partial T/\partial r$) as well as the type of the medium (i.e., κ) for the heat transfer, as [39]

$$\dot{q}_I = -\kappa_I \left.\frac{\partial T}{\partial r}\right|_{R_I}, \quad \dot{q}_O = -\kappa_O \left.\frac{\partial T}{\partial r}\right|_{R_O} \tag{4}$$

where $\dot{q}_I$, κ_I, and $\dot{q}_O$, κ_O represent the heat dissipation rate and the thermal conductivity from the inner and outer surfaces, respectively. The relationship 1 with the boundary conditions given in Eq. (4) does not have a stable solution, since there is a need for a constant value boundary condition. Therefore, solutions for the extreme cases of heat conductivity are assessed and divided into the inner-metallic ($\kappa_I \gg \kappa_O$) and outer-metallic ($\kappa_O \gg \kappa_I$) cases. The generated internal heat needs to pass through the electrolyte and the boundary material in series to dissipate to the environment. In this regard, a metallic boundary typically has orders of magnitude higher thermal conductivity than the electrolyte (i.e., $\kappa_{I,O} \gg \kappa_E$), which means that upon the generation of internal heat and initiation of the heat transfer, it passes the thermal energy through itself at a significantly faster rate than the electrolyte per se, leaving no internal energy inside. Technically this could be phrased as the material with extreme conductivity has thermally short-circuited with the environment, causing the metal to remain nearly at the same temperature as the ambient value. Hence, the boundary condition could be expressed as:

$$\begin{cases} T_I \approx T_\infty & \text{Inner} - \text{metallic} \\ T_O \approx T_\infty & \text{Outer} - \text{metallic} \end{cases} \tag{5}$$

and these boundary conditions should be applied to the respective location of R_I and R_O as shown in Fig. 1(*b*).

2.1 Ordinary Temperature Profile. From the temperature evolution relationship, given in Eq. (1), one can obtain the steady-state profile by setting $\frac{\partial T}{\partial r} \approx 0$. In that case:

$$\frac{d}{dr}\left(r\frac{dT}{dr}\right) + \frac{\dot{q}_{GEN}}{\kappa_E} = 0 \tag{6}$$

where $\kappa_E = \alpha\rho c$ is the thermal conductivity of the electrolyte. For the ordinary disk of radius R, the respective boundary conditions would be the ambient temperature in the outer boundary and the no variation of the temperature in the center due to symmetry, hence

$$T_O = T_\infty, \quad \left.\frac{\partial T}{\partial r}\right|_{r=0} = 0 \tag{7}$$

Integrating Eq. (6) twice, one gets

$$T = -\frac{\dot{q}_{GEN}}{4\kappa_E} r^2 + C_1 \ln(r) + C_2 \tag{8}$$

and applying the boundary conditions from Eq. (7) yields

$$T = -\frac{\dot{q}_{GEN}}{4\kappa_E}(R^2 - r^2) + T_\infty \tag{9}$$

which shows a parabolic temperature distribution, with the maximum value in the center ($r = 0$) obtained as

$$T_{\max} = -\frac{\dot{q}_{GEN}}{4\kappa_E} R^2 + T_\infty$$

2.2 Inner/Outer Metallic Boundary. The inclusion of the heat sink in the center could drastically reduce temperature values including the maximum temperature. In fact, if the temperature in the inner R_I and outer R_O boundaries is T_I and T_O, respectively, relationship 6 will have the following boundary conditions:

$$T_I = T_\infty, \quad T_O = T_\infty \tag{10}$$

2.2.1 Transient Behavior. If T_i^j represents the temperature in the radial distance r_i and the time t_j, the discretization of relationship 1 is obtained as follows:

$$\frac{T_i^{j+1} - T_i^j}{\delta t} = \alpha\left(\frac{T_{i+1}^j - 2T_i^j + T_{i-1}^j}{\delta r^2} + \frac{1}{r_i}\frac{T_{i+1}^j - T_i^j}{\delta r}\right) + \frac{\dot{q}_{GEN}}{\rho C}$$

re-arranging gives:

$$T_i^{j+1} = \left(1 - \frac{2\alpha\delta t}{\delta r^2} - \frac{\alpha\delta t}{r_i \delta r}\right)T_i^j + \left(\frac{2\alpha\delta t}{\delta r^2} + \frac{\alpha\delta t}{r_i\delta r}\right)T_{i+1}^j + \left(\frac{\alpha\delta t}{r_i\delta r^3}\right)T_{i-1}^j + \frac{\dot{q}_{GEN}}{\rho C}\delta t$$

where, in order to have a stable solution, the resolution of the time intervals δt should be fine enough to capture the variation in the space, leading to a stable solution; hence, all the coefficients must be non-negative

$$1 - \frac{2\alpha\delta t}{\delta r^2} - \frac{\alpha\delta t}{r_i\delta r} > 0$$

$$\delta t < \frac{1}{\frac{2\alpha}{\delta r^2} - \frac{\alpha}{r_i\delta r}}$$

In order to satisfy the above relationship $\delta r \ll r_i$

$$\frac{1}{\frac{3\alpha}{\delta r^2}} < \frac{1}{\frac{2\alpha}{\delta r^2} - \frac{\alpha}{r_i\delta r}}$$

Table 1 Physical/computational parameters

Parameter	Value	Unit	Ref.	Parameter	Value	Unit	Ref.
μ_{EC}	2.64	mpa · s	[40]	R_I	1, 2, 5, 10	mm	Assumed
a	0.9	$\dot{A}$	[41,42]	R_O	20	mm	Assumed
i	1	mA.cm^{-2}	[43]	T_O	298	K	Standard
c	1750	J.kg^{-1} · K^{-1}	[44]	$T_{g,EC}$	145	C	[45][1]
l	0.32	cm	[46,47]	δr	150	μm	Assumed
κ_{EC}	0.2	W · m^{-1} · K^{-1}	[48]	δt	6.2	μm	Eq. (11)
ρ_{EC}	1320	kg · m^{-3}	[49]				

[1]https://pubchem.ncbi.nlm.nih.gov/compound/7303#section=Flash-Point

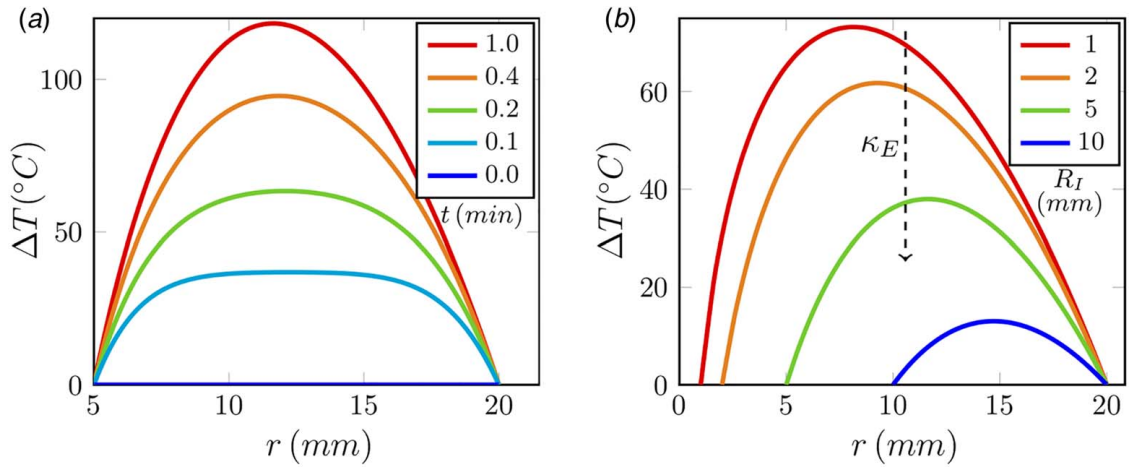

Fig. 2 Temperature profile versus time t, inner radius R_I and the electrolyte diffusivity α

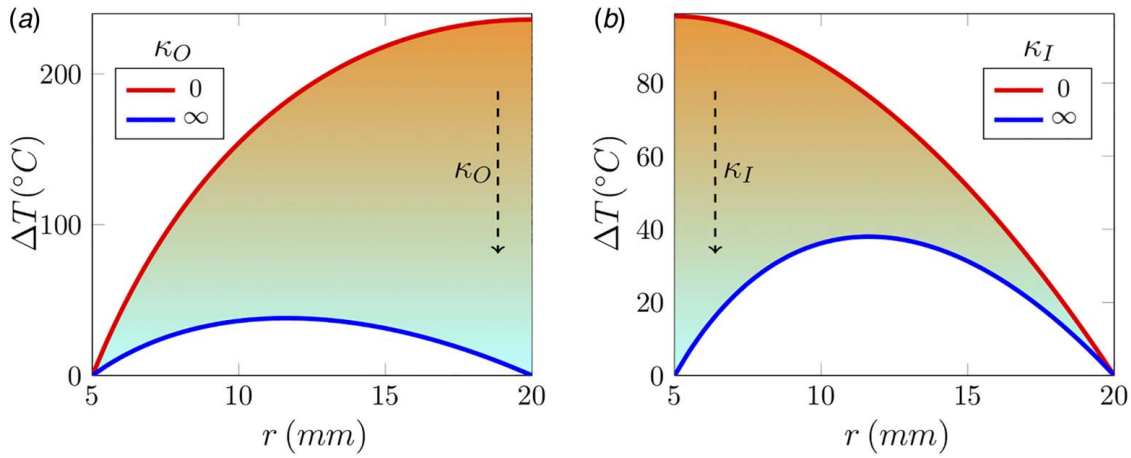

Fig. 3 Steady-state temperature profile formed for all the ranges of inner κ_I and outer κ_O conductivities

Therefore, the sufficient simplified resolution criterion would be

$$\delta t \leq \frac{\delta r^2}{3\alpha} \tag{11}$$

The physical variables for calculating the temperature profiles are given in Table 1. Additionally, the heat diffusivity α, required for the stability criterion in Eq. (11), is calculated as

$$\alpha = \frac{\kappa}{\rho c} = \frac{0.21}{1320 \times 1750} = 9.1 \times 10^{-8} \mathrm{m}^2.\mathrm{s}^{-1}$$

Subsequently, the transient temperature profile is computed using the stability criterion (Eq. (11)), which is illustrated in Fig. 2(*a*) for different times. Consequently, the temperature profile is investigated versus the scale of the inner sink in Fig. 2(*b*). While the established temperature profiles are merely based on the realistic values from the battery components, they explore the role of their variation on the established temperature. As an example, Fig. 2(*a*) shows the direction correlation of the temperature with the charging time in transient state ($t\uparrow \sim T\uparrow$) and Fig. 2(*b*) illustrates the inverse correlation of the temperature with the scale of the central heat dissipator ($R_I\uparrow \sim T\downarrow$).

2.2.2 Transient Behavior. For finding the steady-state temperature profile, double-integrating Eq. (6) and imposing the boundary conditions rom, Eq. (10), leads to

$$\begin{cases} T_\infty = -\dfrac{\dot{q}_{GEN}}{4\kappa_E} R_I^2 + C_1 \ln(R_I) + C_2 \\ T_\infty = -\dfrac{\dot{q}_{GEN}}{4\kappa_E} R_O^2 + C_1 \ln(R_O) + C_2 \end{cases} \tag{12}$$

Replacing into the constant boundary conditions in Eq. (10) simplifies to

$$\Delta T(r) = \frac{\dot{q}_{GEN}}{4\kappa_E} \left(\frac{(R_O^2 - R_I^2)}{\ln\left(\dfrac{R_O}{R_I}\right)} \ln\left(\frac{r}{R_I}\right) - (r^2 - R_I^2) \right) \tag{13}$$

where $\Delta T(r)$ is the rise in temperature with respect to ambient value ($\Delta T(r) = T - T_\infty$).

2.3 Insulating Outer Medium. The insulating outer medium does not transfer the heat ($\kappa_O \to 0$); in this case, the boundary condition changes to

$$T_I = T_\infty, \quad \left.\frac{\partial T}{\partial r}\right|_{R_O} = 0 \tag{14}$$

Double-integrating Eq. (6) and applying the above boundary conditions lead to

$$\Delta T(r) = \frac{\dot{q}_{GEN}}{4\kappa_E} \left(R_O^2 \ln\left(\frac{r}{R_I}\right)^2 - (r^2 - R_I^2) \right) \tag{15}$$

2.4 Insulating Inner Medium. Regarding the insulating inner medium ($\kappa_I \to 0$), hence

$$\left.\frac{\partial T}{\partial r}\right|_{R_I} = 0, \quad T_O = T_\infty \tag{16}$$

similarly double-integrating Eq. (6) gives

$$\Delta T(r) = \frac{\dot{q}_{GEN}}{4\kappa_E} \left(R_O^2 - r^2 + R_I^2 \ln\left(\frac{r}{R_O}\right)^2 \right) \tag{17}$$

The temperature profiles showing the extreme variations of the inner and outer media conductivity are provided in Figs. 3(*a*) and 3(*b*), respectively.

3 Experimental Setup

The experiments were performed using the manually fabricated electrode-sealed sandwich cells (Fig. 4), where the temperature measurements were taken in three distinct locations of center (T_I), mid-radius (T_M), and outside (T_O) using thermocouples as illustrated in Fig. 4 (top and bottom left). The sandwich cells consist of two circular electrodes, fabricated from lithium foil Li^0 as the anode and the lithium cobalt oxide $LiCoO_2$ as the cathode, which are separated by an electrolytic solution. The preparation was carried out as follows:

The lithium foil (Sigma Aldrich, 99.9%, 0.38 mm thickness) was purchased and transferred to the argon-filled glovebox with controlled moisture and oxygen (H_2O, $O_2 < 1$ppm), manufactured by the Changshu Tongrun Electronic Co. Ltd. Subsequently, several electrodes with the diameter of the sand-9" wich cell ($d = 16$) were taken out via punching (purchased from McMaster-Carr) and were rinsed with the dimethoxyethane (DME), which is the cleaning solvent. Moreover, the lithium cobalt oxide (Aldrich, 99.8% trace metals basis) was purchased and similarly prepared for utilization as the counter electrode. The screws, screw-insulators, and nuts (shown in Fig. 4, bottom right), were

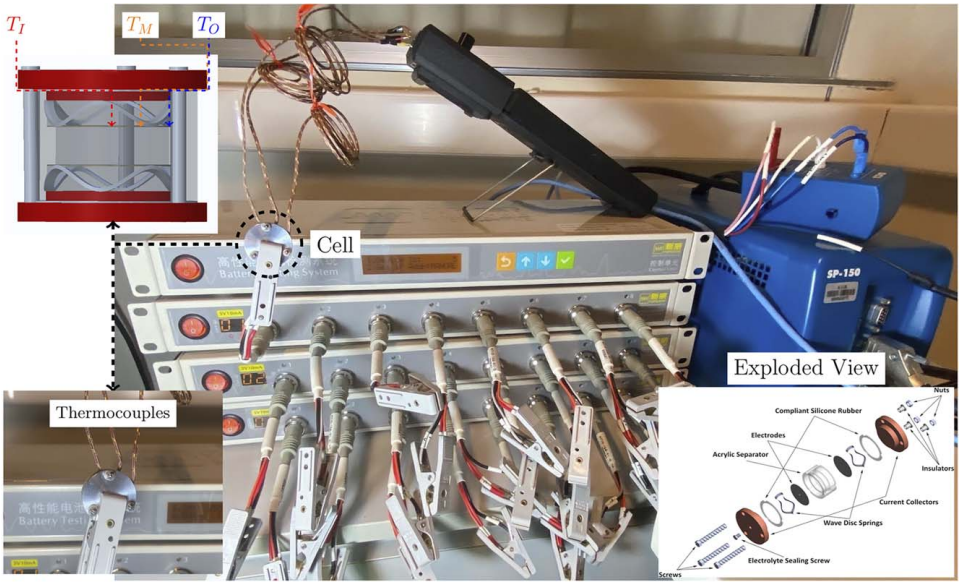

Fig. 4 Experimental setup for the temperature measurements from the different zones of the cell. Top left: the placements of the thermocouple wires; bottom left: zoom into the sandwich battery cell; bottom right: exploded view of the cell components. [50]

purchased from McMaster-carr. The current collectors were precision-machined from an Aluminum plate (purchased from McMaster-carr) to the matching dimensions with the screws and their insulators. As well, the separator housing was first purchased as a plate from McMaster-Carr. Afterward, the laser-cut was used to extract circular rings from it. Finally, the machine mill was utilized to generate circular housing with an intermediate diameter, which matches the diameters of the punched electrodes.

All the sandwich cell components were initially pre-assembled by placing them on top of each other on the table and were fastened via the three screws on the periphery (Fig. 4) [47]. The screws were protected by plastic screw-insulators as sleeves to avoid the electrical short circuit between the opposite current collectors. Furthermore, three thermocouple wires were inserted during the pre-assembled status and were connected to the center, mid-radius, and outside locations to track the local temperature values (Fig. 4, top left and bottom left). Meanwhile, the wave discs were used in-between electrodes and their external packaging to create an insulating space, which gets filled with the gas from the glovebox (i.e., Argon) during the assembly. Such insulation ensures that the heat dissipation from the electrode side is negligible, albeit collecting the current by maintaining point connections between the electrodes and current collectors. The thermal insulation from the electrode side is in fact the extreme case scenario for trapping the heat in batteries, where the dissipation from the boundary becomes the most emphasized.

The electrolyte solution was synthesized by mixing lithium hexafluorophosphate LiPF6 (Aldrich, battery grade, ≥99.99%, trace metals basis) inside the ethylene carbonate EC (Aldrich, Anhydrous, 99%). Consequently, the electrolyte was injected via a syringe in the middle, which was closed and fastened by a wrapped Teflon after.

Multiple cells were fabricated, taken out of the glovebox, and cycled galvanostatically in the multi-channel Neware potentiostat (5mA-10V) with the multitudes of current densities {0.25, 0.5, 0.75}mA.cm^{-2} for 20 cycles. Throughout each experiment, the temperature value started to increase until reaching a steady-state temperature after passing through a transient state. Afterward, the maximum temperature values were recorded, and their average and standard deviation were calculated, where for each point three separate experiments were carried out. Figure 5 visualizes and compares the obtained experimental values, versus the analytical temperature profile with similar parameters attained from

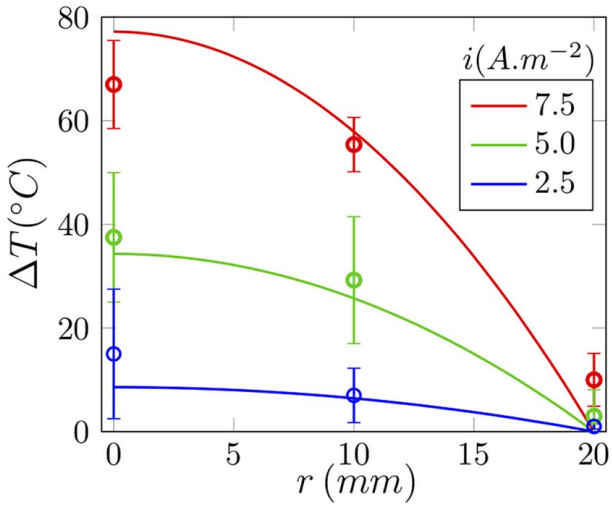

Fig. 5 The steady-state temperature profiles, compared with the experimental values

Eq. (6). The respective close correlations show consistency with our earlier formulation, where the central zone is the most critical.

4 Results and Discussions

The evolution of the temperature described in Eq. (1) is in fact the result of the competition of the generation (i.e., build-up) and the dissipation (i.e., loss) of the heat throughout the time, shown below

$$\left(\frac{\partial T}{\partial t}\right)_{TOT} = \left(\frac{\partial T}{\partial t}\right)_{GEN} + \left(\frac{\partial T}{\partial t}\right)_{DIS}$$

In fact, having the wholistic domain, one could break it down as the following:

$$\begin{cases} \left(\dfrac{\partial T}{\partial t}\right)_{GEN} = \dfrac{\dot{q}_{GEN}}{\rho c} \\ \left(\dfrac{\partial T}{\partial t}\right)_{DIS} = \alpha\left(\dfrac{\partial^2 T}{\partial r^2} + \dfrac{1}{r}\dfrac{\partial T}{\partial r}\right) \end{cases}$$

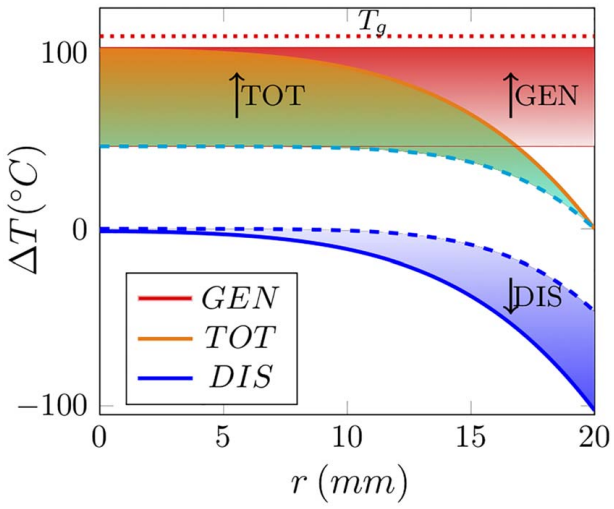

Fig. 6 The competition between the profiles of heat generation (*GEN*) versus dissipation (*DIS*) terms, forming the resultant temperature profile (*TOT*). The arrows indicate the variation in time.

In fact, the rate of heat generation remains constant by the current density, while the dissipation rate grows by the magnitude of the temperature and its gradient in the boundary with the ambient value, until both terms equalize finally in the steady-state regime, as shown in Fig. 2(*a*). More specifically, the slope and curvature of the temperature profile determine the dissipation rate, which is the highest in the steady-state regime. Such variations are visualized in Fig. 6 for an intermediate time(dashed) as well as steady-state condition (solid). While the generation term (GEN) favors the build-up of the temperature, the gradient of temperature between the inside and outside tends to increase the dissipation term (DIS) overtime, mostly in the outer boundary, leading to the formation of the steady-state total temperature profile (TOT).

Additionally, the stability criterion given in Eq. (11) shows a finer segmentation of time versus space relative to the flat geometry with the typical resolution of $\delta t \leq \frac{\delta r^2}{2\alpha}$ [37]. This is due to the higher sensitivity of variation in polar coordinates than the planar, since moving closer to the center squeezes the space to smaller segmentations with higher time precision.

The analytical relationship in Eq. (13) provides the possibility of locating the zone of maximum achievable temperature by setting $\left.\frac{\partial T}{\partial r}\right|_{r_{max}} = 0$ where

$$\frac{dT}{dr} = -2r + \frac{(R_O^2 - R_I^2)}{\ln\left(\frac{R_O}{R_I}\right)}\frac{1}{r} = 0$$

and the location of maximum temperature $r_{\max}$ is obtained as

$$r_{\max} = \sqrt{\frac{R_O^2 - R_I^2}{2\ln\left(\frac{R_o}{R_I}\right)}} \tag{18}$$

The maximum temperature rise $\Delta T_{\max}$ is respectively attained as:

$$\Delta T_{\max} = \frac{\dot{q}_{GEN}}{4\kappa_E}\left(R_I^2 + \frac{R_O^2 - R_I^2}{2\ln\left(\frac{R_o}{R_I}\right)}\ln\left(\frac{R_O^2 - R_I^2}{R_I^2\ln\left(\frac{R_o}{R_I}\right)^{2e}}\right)\right) \tag{19}$$

Herein, we explore if the maximum temperature $r_{\max}$ falls within the inner half of the battery, which compared to the average radius r_{ave} and defining $\hat{R} := \frac{R_O}{R_I}$ yields

$$\sqrt{\frac{\hat{R}^2 - 1}{2\ln(\hat{R})}} < \frac{1}{2}(\hat{R}^2 + 1) \tag{20}$$

simplifying leads to quadratic form as below

$$\left(1 - \frac{\ln(\hat{R})}{2}\right)\hat{R}^2 - \ln(\hat{R}).\hat{R} - 1 - \frac{\ln(\hat{R})}{2} < 0 \tag{21}$$

herein, the two possibilities arise, based on the sign of the first coefficient:

(1) $1 - \frac{\ln(\hat{R})}{2} \leq 0$: since $\hat{R} > 0$, all the terms remain negative, and the inequality is always true.
Therefore:

$$\hat{R} \geq e^2 \tag{22}$$

(2) For the case $1 - \frac{\ln(\hat{R})}{2} > 0$, the roots are found as

$$\Delta = (\ln(\hat{R}))^2 + 4\left(1 - \left(\frac{\ln(\hat{R})}{2}\right)^2\right) = 4$$

$$\hat{R} = \frac{\ln(\hat{R}) \pm 2}{2 - \ln(\hat{R})} = \begin{cases} \frac{2 + \ln(\hat{R})}{2 - \ln(\hat{R})} & \text{Larger} \\ -1 & \text{Smaller} \end{cases}$$

Since the quadratic equation is curving-up, the only case for negativity should fall between the roots

$$-1 < \hat{R} \leq \frac{2 + \ln(\hat{R})}{2 - \ln(\hat{R})}$$

The left side of inequality is obvious, since $\hat{R} > 1$. Since in this case $1 < R < e^2$, $1 < \frac{2 + \ln(\hat{R})}{2 - \ln(\hat{R})} < \infty$. Therefore, the RHS of the above inequality can get indefinitely larger and the inequality is already satisfied. Hence:

$$1 < \hat{R} < e^2 \tag{23}$$

From Eqs. (22) and (23), since $\hat{R}$ covers all the possible ranges, we have

$$1 < \hat{R} < \infty \ \surd$$

and Eq. (20) is always true for any given range of $\hat{R}$.

Thus, the maximum temperature always falls inside the inner half of the cell ($r_{\max} < r_{ave}$). As well it is obvious from the scale analysis in Fig. 7 that the maximum location moves relatively further inside with respect to the scale ($\hat{r}_{\max}/\hat{r}_{ave}$ reduces with the cell size). Moreover, while the maximum temperature $T_{\max}$ in Eq. (19) shows a no-linear relationship with the geometry (R_O, R_I, and m), it is linearly proportional to the rate of heat generation $\dot{q}_{GEN}$ and correlates inversely with the heat conductivity of the electrolyte κ_E as

$$\dot{q}_{GEN} \uparrow \sim T_{\max} \uparrow \ , \ \kappa_E \uparrow \sim T_{\max} \downarrow$$

Therefore, higher electrolyte heat conductivity κ_E (as well as higher heat diffusivity α, specific heat capacity c and density ρ, since $\kappa_E = \alpha\rho c$) leads to higher heat dissipation, forming a more alleviated temperature profile. On the other hand, it is physically obvious that the larger radius of the heat sink R_I provides higher dissipation and the maximum temperature gets reduced, as shown in Fig. 2(*b*).

The percent error *Err* for the temperature correlation between the theoretical profile T_{THE} and experimental measurements T_{EXP}, which is visualized in Fig. 5, can be calculated as

$$Err = \frac{1}{3}\sum_i \frac{|T_{THE,i} - T_{EXP,i}|}{T_{THE,i}}$$

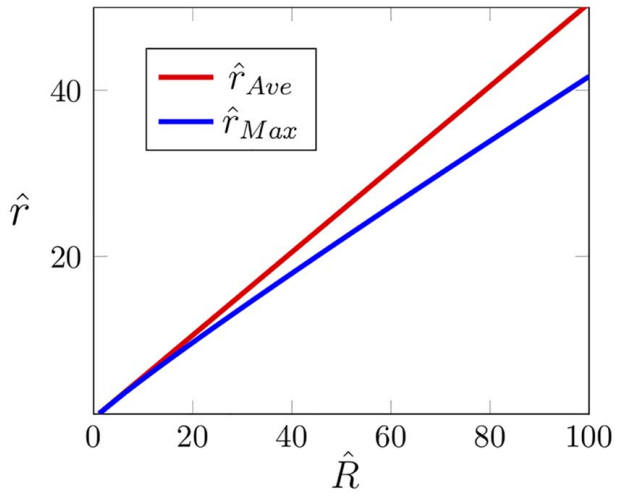

Fig. 7 Comparison of $\hat{r}_{max}$ and $\hat{r}_{ave}$

and is obtained as {8.3%, 4.9%, 4.3%} for the current densities of $\{2.5, 5.0, 7.5\}A.m^{-2}$, respectively, which is in the acceptable range. The possible error source for the higher theoretical number would be not considering the dissipation from the electrode side or not considering the convection as another method of heat transfer. As well, the underlying reason for the lower theoretical temperature could be the limited experimental thermal conductivity in the boundary, which causes more temperature build-up with respect to the modeling.

Finally, it is obvious the maximum temperature $T_{\max}$ is highest when the boundaries become insulating (Figs. 3(*a*) and 3(*b*)). Such difference particularly is the highest for the outer-insulating medium and the underlying reason would be the higher surface area for heat dissipation than the inner boundary ($R_O > R_I$). Needless to mention that if the assembled battery was not sealed, the heat dissipation would additionally occur from the surface of the electrode as well, where two additional boundary conditions occur as follows:

$$\dot{q}_{\text{Bot}} = -\kappa_{Bot}\left.\frac{\partial T}{\partial y}\right|_{y=0}, \quad \dot{q}_{\text{Top}} = -\kappa_{Top}\left.\frac{\partial T}{\partial y}\right|_{y=1}$$

where y is the variable for the vertical distance and $\dot{q}_{\text{Bot}}$, $\dot{q}_{\text{Top}}$ and κ_{Bot}, κ_{Top} are the rate of heat dissipation and heat conductivities of the top and bottom boundaries, respectively.

5 Conclusions

In this paper, a new design was proposed for the effective heat dissipation from the most critical zone (i.e., center) of the electrode-sealed batteries and was analyzed versus the physical (i.e., thermal conductivity) and geometrical (i.e., scale) properties. After the initial calculation of the transient evolution of the temperature distribution, the steady-state profile was analytically obtained. In the next step, the original experiments were performed on the manually fabricated sealed sandwich batteries which formed substantially high temperatures in the central zone. Subsequently, a central metallic heat sink was implemented, which forks out the heat from in/out plane directions, and the respective location and the drop of the (maximum) temperature was quantified. It was analytically proven that for any scale of the heat-dissipating element, the maximum temperature falls closer to the center than the periphery of the cell, which relatively moves further inside with the scale. Furthermore, it is illustrated that due to the curved boundaries, a lower resolution of time-to-space (≈ 33%) is required relative to the flat surfaces for capturing the transient temperature evolution. Finally, it was deciphered that the temperature build-up is in terms of the competitive elements of heat generation from the current density and dissipation due to temperature gradient from the boundaries. The obtained extremums and the respective analysis can be used for the effective design of performance measures for the temperature control during the charging period of the batteries, particularly for those involved in packed clusters or fabricated with recyclable packaging, where the heat has the least possibility to escape.

Acknowledgment

The authors would like to thank the support from Masri Institute at American University of Beirut, Grant Award No. 103919 for the Research Assistant Fadi Elias.

Conflict of Interest

The authors declare that they have no competing financial interests to influence the work reported in this paper.

Data Availability Statement

The row data for producing the results in the paper are freely available upon request from the corresponding author at aryanfar@caltech.edu.

Nomenclature

κ_E = electrolyte thermal cond. ($W \cdot m^{-1} \cdot K^{-1}$)
ρ = electrolyte density ($kg \cdot m^{-3}$)
t = time (s)
v = velocity of ionic transfer ($m \cdot s^{-1}$)
F_d = Drag force on the charge carriers (N)
δr = radial segmentation (m)
δt = time segmentation (s)
R_I = inner radius of the cell (m)
R_O = outer radius of the cell (m)
μ = v viscosity of $LiPF_6$ ($mpa \cdot s$)
a = ionic radius of Li^+ (Å)
i = current density ($A \cdot m^{-2}$)
A = electrode area (m^2)
Q = amount of charge (C)
α = thermal diffusivity ($m^2 s^{-1}$)
T = absolute temperature (K)
r = radial spatial coordinate (m)
c = specific heat ($J \cdot kg \cdot K^{-1}$)
T_g = flash point (K)
ΔT = temperature rise ($T - T_\infty$)

References

[1] Shalf, J., 2020, "The Future of Computing Beyond Moores Law," Philos. Trans. R. Soc. A, **378**(2166), p. 20190061.
[2] Tollefson, J., 2008, "Charging up the Future: A New Generation of Lithium-Ion Batteries, Coupled With Rising Oil Prices and the Need to Address Climate Change, Has Sparked a Global Race to Electrify Transportation," Nature, **456**(7221), pp. 436–441.
[3] Flipsen, S. F. J., 2006, "Power Sources Compared: The Ultimate Truth?," J. Power Sources, **162**(2), pp. 927–934.
[4] Crabtree, G., Kócs, E., and Trahey, L., 2015, "The Energy-Storage Frontier: Lithium-Ion Batteries and Beyond," MRS Bull., **40**(12), pp. 1067–1078.
[5] Hall, P. J., and Bain, E. J., 2008, "Energy-Storage Technologies and Electricity Generation," Energy Policy, **36**(12), pp. 4352–4355.
[6] Ouyang, D., Chen, M., Huang, Q., Weng, J., Wang, Z., and Wang, J., 2019, "A Review on the Thermal Hazards of the Lithium-Ion Battery and the Corresponding Countermeasures," Appl. Sci., **9**(12), p. 2483.
[7] Xu, X. M., and He, R., 2014, "Review on the Heat Dissipation Performance of Battery Pack With Different Structures and Operation Conditions," Renew. Sustainable Energy Rev., **29**, pp. 301–315.
[8] Liu, X., Stoliarov, S. I., Denlinger, M., Masias, A., and Snyder, K., 2015, "Comprehensive Calorimetry of the Thermally-Induced Failure of a Lithium ion Battery," J. Power Sources, **280**, pp. 516–525.

[9] Fu, Y., Lu, S., Li, K., Liu, C., Cheng, X., and Zhang, H., 2015, "An Experimental Study on Burning Behaviors of 18650 Lithium Ion Batteries Using a Cone Calorimeter," J. Power Sources, **273**, pp. 216–222.
[10] Jin, C., Sun, Y., Wang, H., Lai, X., Wang, S., Chen, S., Rui, X., Zheng, Y., Feng, X., Wang, H., et al., 2021, "Model and Experiments to Investigate Thermal Runaway Characterization of Lithium-Ion Batteries Induced by External Heating Method," J. Power Sources, **504**, p. 230065.
[11] Lei, Z., Maotao, Z., Xiaoming, X., and Junkui, G., 2019, "Thermal Runaway Characteristics on NCM Lithium-Ion Batteries Triggered by Local Heating Under Different Heat Dissipation Conditions," Appl. Therm. Eng., **159**, p. 113847.
[12] Liang, C., Jiang, L., Ye, S., Wang, Z., Wei, Z., Wang, Q., and Sun, J., 2021, "Precise In-Situ and Ex-Situ Study on Thermal Behavior of lini1/3co1/3mn1/3o2/Graphite Coin Cell: From Part to the Whole Cell," J. Energy Chem., **54**, pp. 332–341.
[13] Leising, R. A., Palazzo, M. J., Takeuchi, E. S., and Takeuchi, K. J., 2001, "A Study of the Overcharge Reaction of Lithium-Ion Batteries," J. Power Sources, **97**, pp. 681–683.
[14] Strobridge, F. C., Orvananos, B., Croft, M., Yu, H.-C., Robert, R., Liu, H., Zhong, Z., Connolley, T., Drakopoulos, M., Thornton, K., et al., 2015, "Mapping the Inhomogeneous Electrochemical Reaction Through Porous lifepo4-Electrodes in a Standard Coin Cell Battery," Chem. Mater., **27**(7), pp. 2374–2386.
[15] Park, S., Savvides, A., and Srivastava, M. B., 2001, "Battery Capacity Measurement and Analysis Using Lithium Coin Cell Battery," ISLPED'01: Proceedings of the 2001 International Symposium on Low Power Electronics and Design (IEEE Cat. No. 01TH8581), Huntington Beach, CA, Aug. 6–7, IEEE, pp. 382–387.
[16] Zhang, J., and Lu, W., 2022, "Sparse Data Machine Learning for Battery Health Estimation and Optimal Design Incorporating Material Characteristics," Appl. Energy, **307**, p. 118165.
[17] Zhang, Y., and Harb, J. N., 2013, "Performance Characteristics of Lithium Coin Cells for Use in Wireless Sensing Systems: Transient Behavior During Pulse Discharge," J. Power Sources, **229**, pp. 299–307.
[18] Liang, C., Jiang, L., Ye, S., Sun, J., and Wang, Q., 2019, "Comprehensive Analysis on Dynamic Heat Generation of lini1/3co1/3mn1/3o2 Coin Cell Under Overcharge," J. Electrochem. Soc., **166**(14), pp. A3369–A3376.
[19] Rodrigues, M.-T. F., Kalaga, K., Gullapalli, H., Babu, G., Mohana Reddy, A. L., and Ajayan, P. M., 2016, "Hexagonal Boron Nitride-Based Electrolyte Composite for Li-Ion Battery Operation From Room Temperature to 150Â° c," Adv. Energy Mater., **6**(12), p. 1600218.
[20] Fayaz, H., Afzal, A., Samee, A. D. M., Soudagar, M. E. M., Akram, N., Mu- jtaba, M. A., Jilte, R. D., Islam, M. T., Ağbulut, Ü., and Sasleel, C. A., 2022, "Optimization of Thermal and Structural Design in Lithium-Ion Batteries to Obtain Energy Efficient Battery Thermal Management System (Btms): A Critical Review," Archiv. Comput. Methods Eng., **29**(1), pp. 129–194.
[21] Li, W., Peng, X., Xiao, M., Garg, A., and Gao, L., 2019, "Multi-objective Design Optimization for Mini-Channel Cooling Battery Thermal Management System in an Electric Vehicle," Int. J. Energy Res., **43**(8), pp. 3668–3680.
[22] Wu, M.-S., Liu, K. H., Wang, Y.-Y., and Wan, C.-C., 2002, "Heat Dissipation Design for Lithium-Ion Batteries," J. Power Sources, **109**(1), pp. 160–166.
[23] Wang, P., Xinyi Zhang, L. Y., Zhang, X., Yang, M., Chen, H., and Fang, D., 2016, "Real-Time Monitoring of Internal Temperature Evolution of the Lithium-Ion Coin Cell Battery During the Charge and Discharge Process," Extrem. Mech. Lett., **9**, pp. 459–466.
[24] Yang, Y., Okonkwo, E. G., Huang, G., Xu, S., Sun, W., and He, Y., 2021, "On the Sustainability of Lithium Ion Battery Industry–A Review and Perspective," Energy Storage Mater., **36**, pp. 186–212.
[25] Sarkar, D., Shah, K., Haji-Sheikh, A., and Jain, A., 2014, "Analytical Modeling of Temperature Distribution in an Anisotropic Cylinder With Circumferentially-Varying Convective Heat Transfer," Int. J. Heat Mass Transfer, **79**, pp. 1027–1033.
[26] Anthony, D., Sarkar, D., and Jain, A., 2016, "Non-Invasive, Transient Determination of the Core Temperature of a Heat-Generating Solid Body," Sci. Rep., **6**(1), pp. 1–10. URL: .
[27] Zhou, L., Parhizi, M., and Jain, A., 2021, "Temperature Distribution in a Multi-Layer Cylinder With Circumferentially-Varying Convective Heat Transfer Boundary Conditions," Int. J. Therm. Sci., **160**, p. 106673.
[28] Bernagozzi, M., Georgoulas, A., Miche, N., and Marengo, M., 2022, "Heat Pipes in Battery Thermal Management Systems for Electric Vehicles: A Critical Review," Appl. Therm. Eng., **219**, Part A, p. 119495.
[29] Wang, Y., Dan, D., Zhang, Y., Qian, Y., Panchal, S., Fowler, M., Li, W., Tran, M.-K., and Xie, Y., 2022, "A Novel Heat Dissipation Structure Based on Flat Heat Pipe for Battery Thermal Management System," Int. J. Energy Res., **46**(11), pp. 15961–15980.
[30] Han, X., Wang, X., Zheng, H., Xu, X., and Chen, G., 2016, "Review of the Development of Pulsating Heat Pipe for Heat Dissipation," Renew. Sustainable Energy Rev., **59**, pp. 692–709.
[31] Patil, M. S., Seo, J.-H., Panchal, S., and Lee, M.-Y., 2021, "Numerical Study on Sensitivity Analysis of Factors Influencing Liquid Cooling With Double Cold-Plate for Lithium-Ion Pouch Cell," Int. J. Energy Res., **45**(2), pp. 2533–2559.
[32] Duan, J., Zhao, J., Li, X., Panchal, S., Yuan, J., Fraser, R., and Fowler, M., 2021, "Modeling and Analysis of Heat Dissipation for Liquid Cooling Lithium-Ion Batteries," Energies, **14**(14), p. 4187.
[33] Choudhari, V. G., Dhoble, A. S., and Panchal, S., 2020, "Numerical Analysis of Different fin Structures in Phase Change Material Module for Battery Thermal Management System and Its Optimization," Int. J. Heat Mass Transfer, **163**, p. 120434.
[34] Bonnick, P., and Dahn, J. R., 2012, "A Simple Coin Cell Design for Testing Rechargeable Zinc-Air or Alkaline Battery Systems," J. Electrochem. Soc., **159**(7), pp. A981–A989.
[35] Nitta, N., Wu, F., Lee, J. T., and Yushin, G., 2015, "Li-Ion Battery Materials: Present and Future," Mater. Today, **18**(5), pp. 252–264.
[36] Samimi, F., Babapoor, A., Azizi, M., and Karimi, G., 2016, "Thermal Management Analysis of a Li-Ion Battery Cell Using Phase Change Material Loaded With Carbon Fibers," Energy, **96**, pp. 355–371.
[37] Incropera, F. P., DeWitt, D. P., Bergman, T. L., Lavine, A. S., et al., 1996, *Fundamentals of Heat and Mass Transfer*, 6th Ed., Wiley, New York.
[38] Shaughnessy, E. J., Katz, I. M., and Schaffer, J. P., 2005, *Introduction to Fluid Mechanics, Volume 8*, Oxford University Press, New York.
[39] Logan, E. R., Tonita, E. M., Gering, K. L., Ma, L., Bauer, M. K. G., Li, J., Beaulieu, L. Y., and Dahn, J. R., 2018, "A Study of the Transport Properties of Ethylene Carbonate-Free Li Electrolytes," J. Electrochem. Soc., **165**(3), pp. A705–A716.
[40] Aryanfar, A., Medlej, S., and Goddard III, W. A., 2021, "Morphometry of Dendritic Materials in Rechargeable Batteries," J. Power Sources, **481**, p. 228914.
[41] Shannon, R. D., 1976, "Revised Effective Ionic Radii and Systematic Studies of Interatomic Distances in Halides and Chalcogenides," Acta Crystallogr. Sect., A, **32**(5), pp. 751–767.
[42] Orsini, F., Pasquier, A. D., Beaudoin, B., and Tarascon, J. M., 1998, "In Situ Scanning Electron Microscopy (SEM) Observation of Interfaces With Plastic Lithium Batteries," J. Power Sources, **76**(1), pp. 19–29.
[43] Lemmon, E. W., Huber, M. L., McLinden, M. O., et al. Nist Standard Reference Database 23. Reference Fluid Thermodynamic and Transport Properties (REFPROP), Version, 9, 2010.
[44] Hess, S., Wohlfahrt-Mehrens, M., and Wachtler, M., 2015, "Flammability of Li-Ion Battery Electrolytes: Flash Point and Self-Extinguishing Time Measurements," J. Electrochem. Soc., **162**(2), pp. A3084–A3097.
[45] Narayanan, S. R., Surampudi, S., Attia, A. I., and Bankston, C. P., 1991, "Analysis of Redox Additive-Based Overcharge Protection for Rechargeable Lithium Batteries," J. Electrochem. Soc., **138**(8), pp. 2224–2229.
[46] Aryanfar, A., Brooks, D., Merinov, B. V., Goddard Iii, W. A., Colussi, A. J., and Hoffmann, M. R., 2014, "Dynamics of Lithium Dendrite Growth and Inhibition: Pulse Charging Experiments and Monte Carlo Calculations," J. Phys. Chem. Lett., **5**(10), pp. 1721–1726.
[47] Johnson, P. H., 1985, *The Properties of Ethylene Carbonate and Its Use in Electrochemical Applications: A Literature Review*, Lawrence Berkeley National Laboratory, Berkeley, CA, p. 19886.
[48] Weaver, J. H., and Frederikse, H. P. R., 1977, *CRC Handbook of Chemistry and Physics*, CRC Press, Boca Raton, FL, 12–156, 76.
[49] Byron Bird, R., Stewart, W. E., and Lightfoot, E. N., 1960, *Transport Phenomena*, John Wiley and Sons, New York.
[50] Aryanfar, A. Method and Device for Dendrite Research and Discovery in Batteries, April 11, 2017. US Patent No. 9,620,808.